Centrum voor Wiskunde en Informatica
REPORT*RAPPORT*

Large-Eddy Simulation with Accurate Implicit Subgrid-Scale Diffusion

C. Beets, B. Koren

Department of Numerical Mathematics

NM-R9601 1996

Report NM-R9623
ISSN 0169-0388

CWI
P.O. Box 94079
1090 GB Amsterdam
The Netherlands

Large-Eddy Simulation with Accurate Implicit Subgrid-Scale Diffusion

Cees Beets
IMAU
P.O. Box 80005, 3508 TA Utrecht, The Netherlands

Barry Koren
CWI
P.O. Box 94079, 1090 GB Amsterdam, The Netherlands

Abstract

A method for large-eddy simulation is presented that does not use an explicit subgrid-scale diffusion term. Subgrid-scale effects are modelled implicitly through an appropriate monotone discretization method for the advective terms. Special attention is given to the accuracy of the implicit subgrid-scale diffusion term. Computational results are shown for the dispersion of a passive scalar in an artificial turbulent velocity field. Comparisons are made with standard large-eddy simulation results. From the viewpoint of accuracy and computational costs the results are satisfactory.

AMS Subject Classification (1991): 58F22, 65M15, 65M20, 65M60, 76F05
Keywords and Phrases: homogeneous isotropic turbulence, large-eddy simulation, advection-diffusion, subgrid-scale diffusion, monotonicity, accuracy, periodic solutions.
Note: This report will be published elsewhere. The research reported was performed as part of CWI's and IMAU's CIRK-project.

1 Introduction

The principles of large-eddy simulation (LES) are summarized in section 1.1 for the dispersion of a passive scalar in a turbulent velocity field. Based on that summary, in section 1.2 the principles of the present alternative LES approach are given. The alternative approach was first presented in Boris *et al.* (1992). There it was named monotone integrated large-eddy simulation (MILES). In section 2 we consider in more detail the specific LES and MILES schemes to be considered in this paper. First, in section 2.1, we present advection and diffusion schemes to be applied in LES. Second, in section 2.2 we derive a discretization method for advection that implicitly includes a subgrid-scale diffusion term. Next a test problem is defined (section 3.1) and computational results are presented (section 3.2). The paper ends with concluding remarks and suggestions for further research (section 4).

1.1 The LES approach

The conservation equation with constant Fickian diffusion constant D, for a passive species $c(\mathbf{x},t)$ which is transported by a velocity field $\mathbf{v}(\mathbf{x},t)$, is given by

$$\frac{\partial c}{\partial t} + \nabla \cdot (c\mathbf{v}) - D\nabla^2 c = 0. \tag{1.1}$$

If the velocity field is turbulent, it covers a range of length scales which extends from the physical domain's length scale L, down to the Kolmogorov microscale η, which is given by

$$\eta = \left(\frac{\nu^3}{\bar{\epsilon}}\right)^{\frac{1}{4}}, \tag{1.2}$$

where ν is the kinematic viscosity, and $\overline{\epsilon}$ the ensemble-mean dissipation rate of kinetic energy. (Bars denote ensemble-mean values.) The ratio L/η is proportional to $Re^{\frac{3}{4}}$, Re being the Reynolds number. If Re is not too large, present-day computational means enable direct numerical simulation (DNS) of all length scales. However, for high-Reynolds-number flows, it is still practically impossible to solve the entire range of length scales from η to L. Filtering (1.1) with a low-pass spatial filter (cf. e.g. Deardorff 1970) is one way to overcome this problem:

$$\frac{\partial \hat{c}}{\partial t} + \nabla \cdot (\hat{c}\hat{\mathbf{v}}) + \nabla \cdot (\widehat{c\mathbf{v}} - \hat{c}\hat{\mathbf{v}}) - D\nabla^2 \hat{c} = 0. \tag{1.3}$$

In here terms with hat are spatially filtered terms. The large-scale scalar field $\hat{c}$ can be solved with an acceptable resolution, because the subgrid scales of the scalar field are filtered out. The low-pass spatial filter that we will use is characterized by a length scale l_f and a corresponding cut-off wave number $\kappa_c \equiv 2\pi/l_f$.

The third term in (1.3), which represents the effect of subgrid-scales upon the large-scale field, has to be modelled. The modelling of this subgrid-scale (SGS) term is the basis of large-eddy simulation (LES). Many of the SGS models used in LES are based upon the so-called gradient-diffusion hypothesis (cf. e.g. Ciofalo 1993). Using this hypothesis the SGS term in (1.3) is modelled by

$$\widehat{c\mathbf{v}} - \hat{c}\hat{\mathbf{v}} = -D_t \nabla \hat{c}, \tag{1.4}$$

where D_t is the so-called SGS eddy diffusivity. Substituting (1.4) into (1.3) gives

$$\frac{\partial \hat{c}}{\partial t} + \nabla \cdot (\hat{c}\hat{\mathbf{v}}) - \nabla \cdot [(D_t + D)\nabla \hat{c}] = 0. \tag{1.5}$$

An expression for the SGS eddy diffusivity D_t will be derived from inertial-subrange theory (cf. e.g. Tennekes & Lumley 1980).

For high-Reynolds-number flows, which are driven at large scales, a so-called inertial-convective subrange exists for wave numbers of magnitude

$$\frac{1}{L} \ll \kappa \ll \frac{1}{\max(\eta, \eta_c)}. \tag{1.6}$$

Here, the microscale η_c is defined by

$$\eta_c = \left(\frac{D^3}{\overline{\epsilon}}\right)^{\frac{1}{4}}. \tag{1.7}$$

Within the inertial-convective subrange the three-dimensional spectra of kinetic energy and scalar variance, integrated over all wave numbers of magnitude κ, are

$$\overline{E}(\kappa) = \alpha \frac{\overline{\epsilon}^{\frac{2}{3}}}{\kappa^{\frac{5}{3}}} \quad \text{and} \tag{1.8a}$$

$$\overline{E_c}(\kappa) = \beta \frac{\overline{\epsilon_c}}{\overline{\epsilon}^{\frac{1}{3}} \kappa^{\frac{5}{3}}} \tag{1.8b}$$

respectively, where the dissipation rates of kinetic energy ϵ and scalar variance ϵ_c are

$$\epsilon = \nu \nabla \mathbf{v} : (\nabla \mathbf{v})^T \quad \text{and} \tag{1.9a}$$

$$\epsilon_c = 2D \nabla c \cdot \nabla c. \tag{1.9b}$$

(The operator : in (1.9a) is the contraction operator defined by $\mathbf{A} : \mathbf{B} = \mathbf{A}_{ik}\mathbf{B}_{ki}$, where $\mathbf{A}$ and $\mathbf{B}$ are matrices.) Measurements can be used to determine the constants α and β in (1.8), e.g. Andreas (1987) indicates that $\alpha \approx 1.6$ and $\beta \approx 0.67$. The one-dimensional spectra $\overline{E^{1D}}(\kappa)$ and $\overline{E_c^{1D}}(\kappa)$ are similar to the three-dimensional spectra, but the coefficients α and β become $\alpha_1 = \frac{18}{55}\alpha$ and $\beta_1 = \frac{3}{5}\beta$ (cf. Hinze, 1975). In the next paragraph (1.8b) will be used to derive an expression for the SGS eddy diffusivity D_t.

The evolution equation for $\hat{c}^2$ (obtained by multiplying (1.5) with $2\hat{c}$ and assuming a solenoidal velocity field),

$$\frac{\partial \hat{c}^2}{\partial t} = \underbrace{-\nabla \cdot (\hat{c}^2 \hat{\mathbf{v}})}_{\text{RT}} + \underbrace{\nabla \cdot (D + D_t) \nabla \hat{c}^2}_{\text{UT}} - \underbrace{2(D + D_t) \nabla \hat{c} \cdot \nabla \hat{c}}_{\text{DI}}, \tag{1.10}$$

reveals the term which represents the dissipation of resolved variance (DI). The other terms in the right-hand side of (1.10) are the resolved and unresolved turbulent transport terms (RT and UT, respectively). If the cut-off wave number κ_c is located within the inertial-convective subrange, i.e. κ_c satisfies (1.6), the ensemble-mean dissipation rate of resolved variance $\overline{\text{DI}}$ is equal to the ensemble-mean dissipation rate of total variance $\overline{\epsilon_c}$. This implies that

$$\overline{\epsilon_c} = -2(D + D_t) \overline{\hat{c} \nabla^2 \hat{c}}, \tag{1.11}$$

if there is no contribution of the ensemble-mean UT term to $\overline{\epsilon_c}$, which is true for isotropic SGS turbulence. Using

$$\overline{c \nabla^2 c} = -\int_0^\infty \kappa^2 \overline{E_c}(\kappa) \mathrm{d}\kappa, \tag{1.12}$$

we can rewrite (1.11) as

$$\overline{\epsilon_c} = 2(D + D_t) \int_0^{\kappa_c} \kappa^2 \overline{E_c}(\kappa) \mathrm{d}\kappa. \tag{1.13}$$

In (1.13) the ensemble-mean spectrum of scalar variance is given by (1.8b), because we assumed that the cut-off wave number κ_c is located within the inertial-convective subrange. We then obtain the following expression for D_t (using $\kappa_c \equiv 2\pi/l_f$):

$$D + D_t = \left(\frac{2}{3\beta}\right) \left(\frac{l_f}{2\pi}\right)^{\frac{4}{3}} \overline{\epsilon}^{\frac{1}{3}}. \tag{1.14}$$

The ensemble-mean dissipation rate of kinetic energy $\overline{\epsilon}$ and the filter length-scale l_f, which appear in (1.14), will be specified in the next paragraph. Notice that the upper limit of integration in (1.13) can no longer be equal to κ_c for $l_f \to 0$ because of the constant diffusion coefficient D. The relations (1.7) and (1.14) demonstrate that for $D_t = 0$ the upper limit of integration becomes:

$$\kappa_u = \left(\frac{2}{3\beta}\right)^{\frac{3}{4}} \frac{1}{\eta_c}. \tag{1.15}$$

In section 3 we will prescribe an artificial turbulent velocity field with a constant ensemble-mean dissipation rate of kinetic energy $\overline{\epsilon} = 1$. This is of course not possible in real flows. However, using the same arguments as above, an estimate for $\overline{\epsilon}$ is readily obtained from

$$\overline{\epsilon} = \left[\left(\frac{3\alpha}{2}\right) \left(\frac{l_f}{2\pi}\right)^{\frac{4}{3}} \hat{S}^2\right]^{\frac{3}{2}}, \tag{1.16}$$

where

$$\hat{S}^2 = \frac{1}{2} \left[\nabla \hat{\mathbf{v}} + (\nabla \hat{\mathbf{v}})^T\right] : \left[\nabla \hat{\mathbf{v}} + (\nabla \hat{\mathbf{v}})^T\right]. \tag{1.17}$$

In LES the filter length-scale l_f which appears in (1.14) is often taken linearly proportional to a characteristic grid size h, in the standard notations from LES literature (cf. Mason 1994):

$$l_f = \frac{C_s}{C_f} h = C_2 h. \tag{1.18}$$

Using (1.14), (1.18), $\beta \approx \frac{2}{3}$ and $\overline{\epsilon} = 1$, (1.5) becomes (assuming $\kappa_c \leq \kappa_u$)

$$\frac{\partial \hat{c}}{\partial t} + \nabla \cdot (\hat{c} \hat{\mathbf{v}}) - \nabla \cdot \left[\left(\frac{C_2 h}{2\pi}\right)^{\frac{4}{3}} \nabla \hat{c}\right] = 0. \tag{1.19}$$

For large values of C_2 the filtered variables $\hat{\mathbf{v}}$ and $\hat{c}$ are sufficiently smooth with respect to the resolution of the numerical scheme, and errors are mainly due to the SGS model. On the other hand, for small values of C_2 numerical errors dominate. In general one wants to tune C_2 such that as many scales as possible are explicitly solved, without the solution getting obscured by numerical errors. Since the SGS model behaves $O(h^{\frac{4}{3}})$, the value of C_2 is generally chosen quite small. A typical value of C_2 used in LES is (cf. Mason 1994)

$$C_2 = \frac{C_s}{C_f} = \frac{0.16}{0.08} = 2. \tag{1.20}$$

Finally an estimate of the SGS variance $\widehat{c^2} - \hat{c}^2$ can be obtained from:

$$\frac{\partial \widehat{c^2} - \hat{c}^2}{\partial t} \approx 2(D + D_t)\nabla\hat{c} \cdot \nabla\hat{c} - \frac{\widehat{c^2} - \hat{c}^2}{{\kappa_c}^{-\frac{2}{3}} - {\kappa_u}^{-\frac{2}{3}}}, \tag{1.21}$$

where, by definition, the production of SGS variance is equal to the dissipation of resolved variance DI, and the dissipation of SGS variance $\widehat{\epsilon_c}$ is estimated from

$$\widehat{\epsilon_c} = \frac{\int_{\kappa_c}^{\kappa_u} \beta \widehat{\epsilon_c} \kappa^{-\frac{5}{3}} \, \mathrm{d}\kappa}{{\kappa_c}^{-\frac{2}{3}} - {\kappa_u}^{-\frac{2}{3}}} \approx \frac{\widehat{c^2} - \hat{c}^2}{{\kappa_c}^{-\frac{2}{3}} - {\kappa_u}^{-\frac{2}{3}}}. \tag{1.22}$$

This completes the presentation of a standard SGS model used in LES.

1.2 The MILES approach

One drawback of LES is that, after a straightforward discretization of (1.19), certain physical properties of (1.1) are still not guaranteed. Important properties of (1.1) are given by the conservation and entropy conditions. Integrating (1.1) over the physical domain Ω, with boundary $\delta\Omega$, the conservation condition can be written as

$$\int_\Omega \frac{\partial c}{\partial t} \, \mathrm{d}\Omega = \int_{\delta\Omega} (-c\mathbf{v} + D\nabla c) \cdot \mathbf{n} \, \mathrm{d}A, \tag{1.23}$$

and the entropy condition as

$$\int_\Omega \frac{\partial c^p}{\partial t} \, \mathrm{d}\Omega = \int_{\delta\Omega} (-c^p \, \mathbf{v} + D\nabla c^p) \cdot \mathbf{n} \, \mathrm{d}A - p(p-1) \int_\Omega D c^{p-2} \left(\frac{\partial c}{\partial x}\right)^2 \mathrm{d}V \ , \quad \forall \, p \in \mathbb{N} \wedge p \geq 2. \tag{1.24}$$

The conservation condition (1.23) implies that, apart from contributions of fluxes at the boundary of the domain, c is conserved. According to the entropy condition (1.24), all the higher moments can only decrease in time if $c \in \mathbb{R}^+$ (again, in the absence of fluxes at the boundary). Other properties that follow from the entropy condition are the total variance diminishing (TVD) property and the positivity property ($c \geq 0 \; \forall \, t > t_0$ if $c \geq 0$ at t_0). (Note: the total *variance* diminishing property differs from the total *variation* diminishing property, which states that $\int_\Omega \mid \nabla c \mid \mathrm{d}\Omega$ can only decrease in time.) These properties can be important, depending upon the particular problem. For example if c is the concentration of a chemically reactive species, a violation of the positivity property can lead to instabilities.

All the spatial discretization methods that will be presented in section 2 satisfy the conservation condition. Some of the spatial discretization methods use a so-called limiter function (cf. Sweby 1984 and Spekreijse 1987) to also satisfy a monotonicity condition. Spekreijse's (1987) definition of monotonicity, which differs from the usual definition of monotonicity, states that (local) minima in space can only increase in time and that (local) maxima can only decrease in time. This is a physical property of (1.1), which is closely related to the entropy condition. Moreover, spatial discretizations which are monotone in Spekreijse's sense prevent the occurrence of non-physical wiggles and negative concentrations. If the semi-discrete conservation equation for c is written as

$$\begin{aligned} \frac{\mathrm{d}c_{i,j,k}}{\mathrm{d}t} &= A_{i,j,k}(c_{i+1,j,k} - c_{i,j,k}) + B_{i,j,k}(c_{i-1,j,k} - c_{i,j,k}) \\ &+ C_{i,j,k}(c_{i,j+1,k} - c_{i,j,k}) + D_{i,j,k}(c_{i,j-1,k} - c_{i,j,k}) \\ &+ E_{i,j,k}(c_{i,j,k+1} - c_{i,j,k}) + F_{i,j,k}(c_{i,j,k-1} - c_{i,j,k}), \end{aligned} \tag{1.25}$$

then Spekreijse's monotonicity condition is

$$0 \leq A_{i,j,k} \ \ldots \ F_{i,j,k} \leq M \quad \forall i,j,k \quad \text{where } M \in (0,\infty). \tag{1.26}$$

(Notice that we use the indices i, j and k as the discrete equivalent of the coordinates x, y and z.) Spekreijse (1987) derived a class of limiter functions which can be used to construct spatial discretizations that satisfy (1.26). Unfortunately his analysis cannot be applied to (1.1) in a straightforward manner. However, in the appendix we will prove that a subset of Spekreijse's class of limiter functions can still be used to guarantee monotonicity.

Boris *et al.* (1992) noticed that when using monotonicity devices, such as limiter functions, a SGS model is no longer essential. Monotone advection schemes add an implicit diffusion term, which acts as a spatial filter. LES without a SGS model was named monotone integrated large-eddy simulation (MILES). So in MILES schemes monotonicity devices have a double role. In our opinion this is also the challenge of MILES schemes. The MILES approach does not avoid the difficulty of resolving the influences of SGS turbulence; this difficulty has only been postponed. Whereas in the LES approach the SGS modelling of turbulence is done in the continuous equations, in the MILES approach it is done in the discrete equations. In this paper we follow the MILES approach. The present work differs from the MILES approach of Boris *et al.* (1992) in that the physical modelling of the implicit diffusion is treated with more accuracy.

2 Discretization methods

2.1 LES discretizations

For the LES approach we consider the one-dimensional advection-diffusion equation, dropping for ease of notation the hats on the symbols:

$$\frac{\partial c}{\partial t} + u\frac{\partial c}{\partial x} - (D + D_t)\frac{\partial^2 c}{\partial x^2} = 0. \tag{2.1}$$

For reasons of transparency u and $(D + D_t)$ are assumed to be constant. Further u is assumed to be positive. Then a cell-centred finite-volume discretization of (2.1) yields the semi-discrete equation

$$\int_{\Omega_i} \frac{\partial c}{\partial t} \mathrm{d}x + u(c_{i+\frac{1}{2}} - c_{i-\frac{1}{2}}) - (D + D_t)\left(\left(\frac{\partial c}{\partial x}\right)_{i+\frac{1}{2}} - \left(\frac{\partial c}{\partial x}\right)_{i-\frac{1}{2}}\right) = 0, \tag{2.2}$$

where the half-integer indices $i - \frac{1}{2}$ and $i + \frac{1}{2}$ refer to the cell faces $\partial\Omega_{i-\frac{1}{2}}$ and $\partial\Omega_{i+\frac{1}{2}}$ between the (full-integer indexed) cell centres Ω_{i-1}, Ω_i and Ω_i, Ω_{i+1}, respectively (figure 1). In the next two sections we

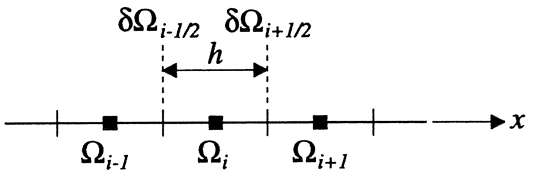

Figure 1: Cell-centred finite volume Ω_i with nearest neighbours.

proceed by presenting four different methods for the evaluation of the advective fluxes and one standard evaluation method for the diffusive fluxes.

2.1.1 Advection

A standard scheme for evaluating the cell-face states is the central second-order accurate scheme:

$$c_{i+\frac{1}{2}} = \frac{1}{2}(c_i + c_{i+1}). \tag{2.3}$$

It can be shown that this scheme conserves the total variance. However, it is not monotone (in the sense of Spekreijse, 1987). Schemes which are monotone (see section 1.2 and the appendix) are the standard first-order upwind scheme:

$$c_{i+\frac{1}{2}} = c_i, \tag{2.4}$$

(similarly $c_{i-\frac{1}{2}} = c_{i-1}$), the not standard, though well-tested, limited $\kappa = \frac{1}{3}$-scheme from Koren (1993):

$$c_{i+\frac{1}{2}} = c_i + \frac{1}{2}\phi(r_{i+\frac{1}{2}})\,(c_i - c_{i-1})\,, \tag{2.5a}$$

$$r_{i+\frac{1}{2}} = \frac{c_{i+1} - c_i}{c_i - c_{i-1}}, \tag{2.5b}$$

$$\phi(r) = \max\left(0, \min\left(2r, \min\left(\frac{1}{3} + \frac{2}{3}r, 2\right)\right)\right), \tag{2.5c}$$

and the new limited $\kappa = -1$-scheme:

$$c_{i+\frac{1}{2}} = c_i + \frac{1}{2}\phi(r_{i+\frac{1}{2}})\,(c_i - c_{i-1})\,, \tag{2.6a}$$

$$r_{i+\frac{1}{2}} = \frac{c_{i+1} - c_i}{c_i - c_{i-1}}, \tag{2.6b}$$

$$\phi(r) = \min(2|r|, 1)\,. \tag{2.6c}$$

In figures 2(a) and 2(b) we depict the limiter functions (2.5c) and (2.6c). Limiter (2.5c) is specifically tailored towards the for accuracy reasons favourable $\kappa = \frac{1}{3}$-scheme. Over the r-range $[\frac{1}{4}, \frac{5}{2}]$ it renders the $\kappa = \frac{1}{3}$-scheme, which latter is known for its good accuracy properties in the class of κ-schemes (cf. Van Leer 1985). For all r except $r \in (-\frac{1}{2}, \frac{1}{2})$, limiter (2.6c) is identical to the $\kappa = -1$-scheme (the second-order accurate, fully one-sided upwind scheme, also see Van Leer 1985). Limiter (2.6c) has a maximum computational simplicity.

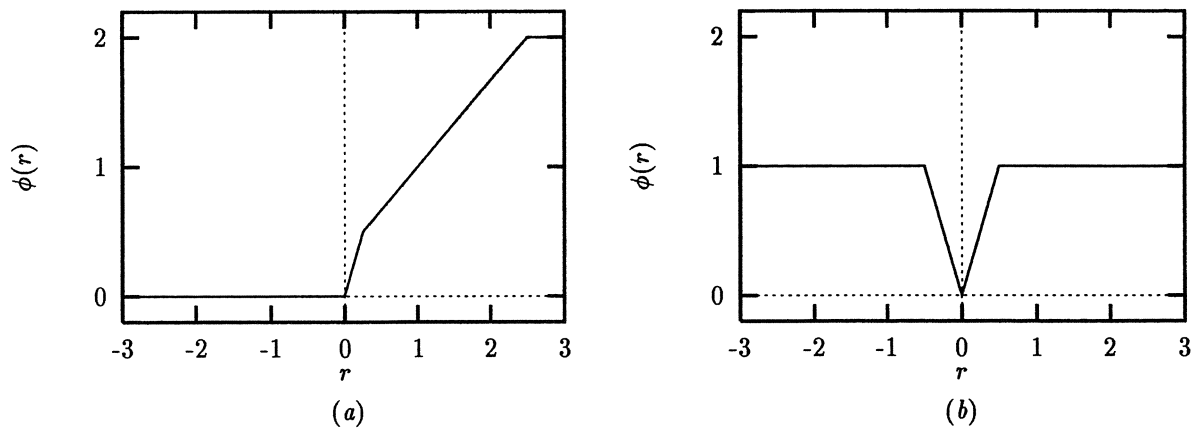

Figure 2: κ-limiters. (a) $\kappa = \frac{1}{3}$-limiter (2.5c) and (b) $\kappa = -1$-limiter (2.6c).

Advection schemes (2.5) and (2.6) cannot be applied straightforward up to and including boundaries with non-periodic conditions imposed on it. In the present paper we only consider a test case with periodic boundary conditions, for which a straightforward application *is* possible.

2.1.2 Diffusion

For the diffusive flux evaluation, the gradient $\left(\frac{\partial c}{\partial x}\right)_{i+\frac{1}{2}}$ (and similarly the gradient $\left(\frac{\partial c}{\partial x}\right)_{i-\frac{1}{2}}$) is evaluated in the standard, second-order accurate central-difference manner

$$\left(\frac{\partial c}{\partial x}\right)_{i+\frac{1}{2}} = \frac{c_{i+1} - c_i}{h}. \tag{2.7}$$

2.2 MILES discretizations

For our present MILES approach we consider the one-dimensional advection equation

$$\frac{\partial c}{\partial t} + u\frac{\partial c}{\partial x} = 0, \tag{2.8}$$

where u is again assumed to be positive and constant. Cell-centred finite-volume discretization (just as in the LES approach) leads next to the semi-discrete equation

$$\int_{\Omega_i} \frac{\partial c}{\partial t} \mathrm{d}x + u(c_{i+\frac{1}{2}} - c_{i-\frac{1}{2}}) = 0. \tag{2.9}$$

Guided by the specific $O(h^{\frac{4}{3}})$-diffusion in (1.19), we derive a monotone, advective discretization with this specific diffusion built in.

2.2.1 Monotonicity

The interpolation for the cell-face state $c_{i+\frac{1}{2}}$ is written as

$$c_{i+\frac{1}{2}} = c_i + \frac{1}{2}\phi(r_{i+\frac{1}{2}}, u, h)\,(c_i - c_{i-1})\,, \tag{2.10}$$

where $\phi(r, u, h)$ is the limiter function, with $r_{i+\frac{1}{2}}$ again the upwind ratio of consecutive solution gradients:

$$r_{i+\frac{1}{2}} \equiv \frac{c_{i+1} - c_i}{c_i - c_{i-1}}. \tag{2.11}$$

Anticipating to the accurate modelling of (1.19), here we take ϕ also dependent on u and h. Still conventionally, $\phi = 0$ and $\phi = 1$ lead to the standard first-order accurate and second-order accurate upwind scheme, respectively. For $0 < \phi < 1$, the resulting scheme is a blend of both standard upwind schemes.

With (2.10), (2.9) becomes

$$\int_{\Omega_i} \frac{\partial c}{\partial t} \mathrm{d}x + u\left[(c_i - c_{i-1}) + \frac{1}{2}\phi(r_{i+\frac{1}{2}}, u, h)(c_i - c_{i-1}) - \frac{1}{2}\phi(r_{i-\frac{1}{2}}, u, h)(c_{i-1} - c_{i-2})\right] = 0, \tag{2.12}$$

which, with $r_{i-\frac{1}{2}} = (c_i - c_{i-1})/(c_{i-1} - c_{i-2})$, can be further rewritten as

$$\int_{\Omega_i} \frac{\partial c}{\partial t} \mathrm{d}x + u\left[1 + \frac{1}{2}\phi(r_{i+\frac{1}{2}}, u, h) - \frac{\frac{1}{2}\phi(r_{i-\frac{1}{2}}, u, h)}{r_{i-\frac{1}{2}}}\right](c_i - c_{i-1}) = 0. \tag{2.13}$$

The monotonicity requirement for the limiter function ϕ which appears in (2.13) is (see section 1.2 and the appendix)

$$0 \le \phi(r, u, h) \le M \quad \wedge \quad -M \le \frac{\phi(r, u, h)}{r} \le 2 \quad \text{where } M \in (0, \infty). \tag{2.14}$$

2.2.2 Subgrid-scale diffusion

In this section, we proceed by imposing to the limiter function the $O(h^{\frac{4}{3}})$-diffusion requirement. The analysis makes use of truncated Taylor-series expansions, which are valid around $r = 1$ only (the region of smooth solutions). Expanding $\phi(r, u, h)$ around $r = 1$ yields

$$\phi(r, u, h) = \phi(1, u, h) + (r - 1)\frac{\partial \phi(1, u, h)}{\partial r} + O\left((r - 1)^2\right). \tag{2.15}$$

With definition (2.11), it is found after Taylor-series expansion

$$r_{i+\frac{1}{2}} - 1 = \frac{h^2 \frac{\partial^2 c}{\partial x^2} + O(h^4)}{h\frac{\partial c}{\partial x} + O(h^2)} = h\frac{\frac{\partial^2 c}{\partial x^2}}{\frac{\partial c}{\partial x}} + O(h^2), \tag{2.16a}$$

and similarly

$$r_{i-\frac{1}{2}} - 1 = \frac{h^2 \frac{\partial^2 c}{\partial x^2} + O(h^3)}{h\frac{\partial c}{\partial x} + O(h^2)} = h\frac{\frac{\partial^2 c}{\partial x^2}}{\frac{\partial c}{\partial x}} + O(h^2). \tag{2.16b}$$

Substitution of (2.16a) and (2.16b) into (2.15) yields

$$\phi(r_{i+\frac{1}{2}}, u, h) = \phi(1, u, h) + h\frac{\frac{\partial^2 c}{\partial x^2}}{\frac{\partial c}{\partial x}}\frac{\partial \phi(1, u, h)}{\partial r} + O(h^2), \tag{2.17a}$$

$$\phi(r_{i-\frac{1}{2}}, u, h) = \phi(1, u, h) + h\frac{\frac{\partial^2 c}{\partial x^2}}{\frac{\partial c}{\partial x}}\frac{\partial \phi(1, u, h)}{\partial r} + O(h^2). \tag{2.17b}$$

Substituting (2.17a) and (2.17b) into (2.12) and expanding the differences $c_i - c_{i-1}$ and $c_{i-1} - c_{i-2}$ in there, then leads to the modified differential equation

$$\frac{\partial c}{\partial t} + u\left[\frac{\partial c}{\partial x} - \frac{h}{2}\left(1 - \phi(1, u, h) - h\frac{\frac{\partial^2 c}{\partial x^2}}{\frac{\partial c}{\partial x}}\frac{\partial \phi(1, u, h)}{\partial r}\right)\frac{\partial^2 c}{\partial x^2}\right] = O(h^2). \tag{2.18}$$

This equation allows us to impose the $O(h^{\frac{4}{3}})$-diffusion requirement. As the specific target equation we consider the one-dimensional version of (1.19) with the velocity constant (to be consistent with the present analysis) and $C_2 = 2$. The target equation then becomes

$$\frac{\partial c}{\partial t} + u\frac{\partial c}{\partial x} - \left(\frac{h}{\pi}\right)^{\frac{4}{3}}\frac{\partial^2 c}{\partial x^2} = 0. \tag{2.19}$$

Equating (2.18) and (2.19), it follows that the limiter must satisfy as the accuracy requirement

$$\phi(1, u, h) = 1 - 2\frac{h^{\frac{1}{3}}}{\pi^{\frac{4}{3}}u}. \tag{2.20}$$

(Note that u- and h-dependence has appeared now.) To still assure the proper diffusion in case $\frac{\partial^2 c}{\partial x^2}/\frac{\partial c}{\partial x} = O(h^{-p}), p \geq \frac{2}{3}$, we also require that

$$\frac{\partial \phi(1, u, h)}{\partial r} = 0. \tag{2.21}$$

A limiter function which satisfies the monotonicity requirement (2.14), as well as the accuracy requirements (2.20) and (2.21), is

$$\phi(r, u, h) = \min\left(2|r|, \min\left(1, 8\frac{h^{\frac{1}{3}}}{\pi^{\frac{4}{3}}u}(r - 1)^2 + 1 - 2\frac{h^{\frac{1}{3}}}{\pi^{\frac{4}{3}}u}\right)\right). \tag{2.22}$$

To avoid negative values of ϕ in case of very small values of u (note that $\phi(1,u,h) < 0$ for $u < \frac{2}{3}h^{\frac{1}{3}}$), for practical purposes we propose the following slightly extended version of (2.22):

$$\phi(r,u,h) = \min\left(2|r|, \min\left(1, \max\left(0, 8\frac{h^{\frac{1}{3}}}{\pi^{\frac{4}{3}}u}(r-1)^2 + 1 - 2\frac{h^{\frac{1}{3}}}{\pi^{\frac{4}{3}}u}\right)\right)\right). \tag{2.23}$$

In figure 3(a), we depict this limiter for $u = 1$ and the mesh-size sequence $h = \frac{1}{2^i 10}, i = 0,1,2,3,4$. A simpler, computationally more efficient form of (2.23), which is comparable to (2.6c) is

$$\phi(r,u,h) = \min\left(2|r|, \min\left(1, \max\left(0, 1 - 2\frac{h^{\frac{1}{3}}}{\pi^{\frac{4}{3}}u}\right)\right)\right). \tag{2.24}$$

In figure 3(b), limiter (2.24) is depicted for $u = 1$ and the mesh-size sequence $h = \frac{1}{2^i 10}, i = 0,1,2,3,4$. In case of variable u ($u = u(x,t)$), for $(\phi(r,u,h))_{\partial\Omega_{i+\frac{1}{2}}}$ we take $\phi(r_{i+\frac{1}{2}}, u_{i+\frac{1}{2}}, h)$. In the next section we will apply limiter (2.24).

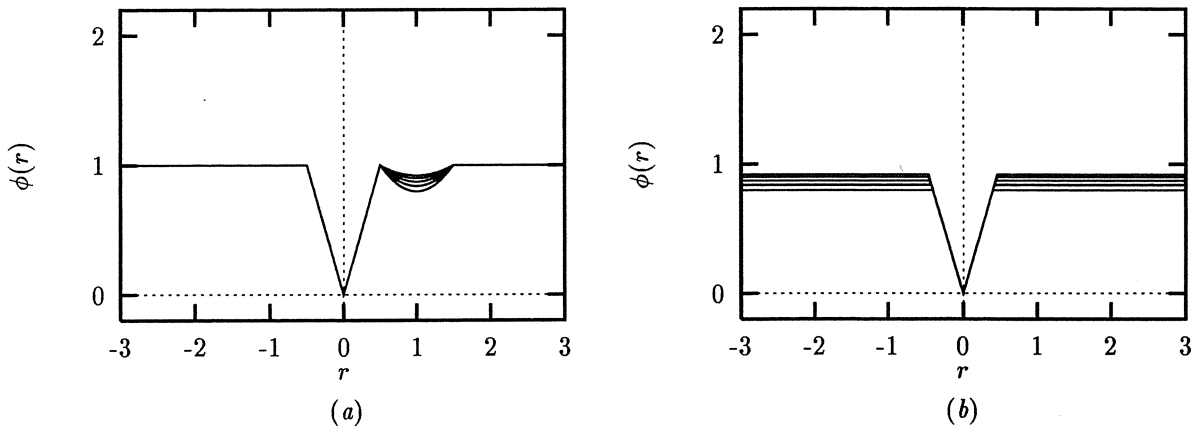

Figure 3: MILES limiters, for $u = 1$ and $h = \frac{1}{2^i 10}, i = 0,1,2,3,4$. ($a$) MILES limiter (2.23) and (b) MILES limiter (2.24).

3 Numerical experiments

3.1 Problem definition

In this section we will apply the spatial discretizations from section 2 to equation (1.19). For the time discretization we will use a second-order accurate Runge-Kutta method. The time step is chosen such that time discretization errors can be neglected compared to spatial discretization errors.

Consider on the domain $0 \leq x,y,z \leq 1$ the scalar c with periodic boundary conditions

$$c(0,y,z,t) = c(1,y,z,t), \tag{3.1a}$$

$$c(x,0,z,t) = c(x,1,z,t), \tag{3.1b}$$

$$c(x,y,0,t) = c(x,y,1,t), \tag{3.1c}$$

and initial datum

$$c(\mathbf{x},0) = \cos(2\pi x)\cos(2\pi y)\cos(2\pi z) + 1. \tag{3.2}$$

For a given filter length scale l_f, (1.19) can then be used to compute the large-scale concentration field for $t > 0$ if a filtered turbulent velocity field $\hat{\mathbf{v}}(\mathbf{x},t)$ is specified.

Here $\hat{\mathbf{v}}(\mathbf{x},t)$ is obtained from a kinematic simulation. (A kinematic simulation uses statistical velocity distributions, that are known from for example DNS, to create artificial turbulent velocity fields.) Since periodic boundary conditions are used, the velocity field can be written as:

$$\mathbf{v}(\mathbf{x},t) = \sum_{\kappa_x,\kappa_y,\kappa_z=2\pi,4\pi\ldots}^{\infty} \int_{-\infty}^{\infty} \mathbf{U}(\kappa_x,\kappa_y,\kappa_z,\omega)\,\cos\left[\kappa_x x+\kappa_y y+\kappa_z z+\omega t+\phi(\kappa_x,\kappa_y,\kappa_z,\omega)\right]\mathrm{d}\omega. \quad (3.3)$$

Following Fung *et al.* (1992) we model the time dependency in the simplest possible way by assuming a single frequency mode for each wave-number mode. Then (3.3) can be rewritten as:

$$\mathbf{v}(\mathbf{x},t) = \sum_{\kappa_x,\kappa_y,\kappa_z=2\pi,4\pi\ldots}^{\infty} \mathbf{U}(\kappa_x,\kappa_y,\kappa_z)\,\cos\left[\kappa_x x+\kappa_y y+\kappa_z z+\omega(\kappa_x,\kappa_y,\kappa_z)t+\phi(\kappa_x,\kappa_y,\kappa_z)\right]. \quad (3.4)$$

We prescribe a constant ensemble-mean dissipation rate of kinetic energy, $\overline{\epsilon}=1$, and an inertial subrange for wave numbers of magnitude $2\pi \le \kappa \le 256\pi$. The rms-velocity U_0 is then equal to

$$U_0 = \sqrt{2\int_{2\pi}^{256\pi} \overline{E}(\kappa)\mathrm{d}\kappa} \overset{(1.8)}{=} \sqrt{2\int_{2\pi}^{256\pi} \alpha\kappa^{-\frac{5}{3}}\mathrm{d}\kappa} \approx 1.16. \quad (3.5)$$

The amplitudes $\mathbf{U}$ in (3.4) are obtained by assigning the total energy of wave numbers with magnitude $\max(2,2n-1)\pi \le \kappa \le \min(256,2n+1)\pi$, where $n=1\ldots128$,

$$E^n = \int_{\max(2,2n-1)\pi}^{\min(256,2n+1)\pi} \alpha\kappa^{-\frac{5}{3}}\mathrm{d}\kappa, \quad (3.6)$$

to a single wave number $(\kappa_x^n,\kappa_y^n,\kappa_z^n)$ which is chosen from a uniform distribution of the discrete wave numbers with magnitude $\max(2,2n-1)\pi \le \kappa \le \min(256,2n+1)\pi$. To ensure that the staggered discrete velocity field is solenoidal we take

$$\mathbf{U}^n = 2\frac{(E^n)^{\frac{1}{2}}}{||\mathbf{k}^n||}\mathbf{k}^n \times \mathbf{u}, \quad (3.7)$$

where $\mathbf{u}$ is a vector which is chosen from an isotropic distribution with magnitude 1, and $\mathbf{k}^n$ is defined by

$$\mathbf{k}^n = \begin{bmatrix} \sin(\frac{1}{2}h_x\kappa_x^n) \\ \sin(\frac{1}{2}h_y\kappa_y^n) \\ \sin(\frac{1}{2}h_z\kappa_z^n) \end{bmatrix}, \quad (3.8)$$

where h_x, h_y and h_z are the (equi-distant) grid spacings in x-, y- and z-direction respectively. For each wave number $(\kappa_x^n,\kappa_y^n,\kappa_z^n)$ a phase ϕ^n is chosen from a uniform probability distribution $[0,2\pi)$, and a frequency ω^n is chosen from a Gaussian probability distribution (Fung *et al.* (1992))

$$P(\omega) = \frac{1}{(2\pi)^{\frac{1}{2}}}\frac{\mathrm{e}^{-\frac{1}{2}(\omega/a\kappa U_0)^2}}{a\kappa U_0}, \quad (3.9)$$

where a is a constant and κ the wave number magnitude. Taking $a=\frac{1}{2}$, the shape of $P(\omega)$ is confirmed by DNS of homogeneous turbulence (cf. Fung *et al.* 1992, p. 295). Using data from wind tunnel measurements, Chase (1970) found $a=1$. Fung *et al.* (1992) argued that this difference is probably due to the low Reynolds number of the DNS simulation. Here we will use $a=1$. Finally we obtain the *filtered* velocity field from

$$\hat{\mathbf{v}}(\mathbf{x},t) = \sum_{n=1}^{\min[128,(hC_2)^{-1}]} \mathbf{U}^n\,\cos\left[\kappa_x^n x+\kappa_y^n y+\kappa_z^n z+\omega^n t+\phi^n\right], \quad (3.10)$$

where we take the characteristic grid size h equal to $(h_x\,h_y\,h_z)^{\frac{1}{3}}$.

The Kolmogorov microscale of the velocity field is approximately equal to $\eta \approx 0.52L/256\pi = 6.5_{10}{}^{-4}$ for $\alpha=1.6$ (cf. Tennekes & Lumley 1980, p. 272), which corresponds to a kinematic viscosity $\nu \approx 5.6_{10}{}^{-5}$ and a Reynolds number $U_0L/\nu = 2.1_{10}{}^4$. We also take $\kappa_u = 256\pi$, which according to (1.15) yields $D \approx 1.33_{10}{}^{-4}$. The Schmidt number $Sc=\nu/D$ is then equal to 0.42.

3.2 Results

In this section we will present results obtained with different resolutions ($16 \times 17 \times 17$, $32 \times 33 \times 33$, $64 \times 65 \times 65$, and $128 \times 129 \times 129$-grids were used) and different values of C_2 ($C_2 = 0, 2$ and 4).

The top panel of figure 4 gives an impression of how the scalar field changes in time. The initial field has values ranging from 0 (black) to 2 (white). As time evolves, regions with low and high values are mixed through diffusion. This mixing is strongly augmented by the velocity field, which generates small scales with high local gradients.

The plots (a), (b) and (c) in the lower panel of figure 4 were obtained after one characteristic time unit $L/U_0 \approx 0.86$. Plots (a) and (b) show the effect of the explicit subgrid-scale (SGS) diffusion term $\nabla \cdot [D_t \nabla \hat{c}]$ (see section 1.1) for the standard second-order central scheme (2.3). It is clear that this SGS term removes the smallest scales. Plot (c) in the lower panel shows that the monotone limited $\kappa = -1$ scheme (2.6), *without* explicit SGS diffusion term, also removes the smallest scales. Compared to the second-order central scheme, the limited $\kappa = -1$ scheme introduces the following additional implicit diffusion term in the x-direction (similar terms are added in the y- and z-direction),

$$D^{art}_{i+\frac{1}{2}} \frac{c_{i+1} - c_i}{h_x^2} - D^{art}_{i-\frac{1}{2}} \frac{c_i - c_{i-1}}{h_x^2}. \tag{3.11}$$

In (3.11) the artificial diffusivity $D^{art}_{i+\frac{1}{2}}$ (and similarly $D^{art}_{i-\frac{1}{2}}$) is given by,

$$D^{art}_{i+\frac{1}{2}} = \frac{1}{2} u^+_{i+\frac{1}{2}} h_x \left(1 - \frac{\phi(r^+_{i+\frac{1}{2}})}{r^+_{i+\frac{1}{2}}} \right) - \frac{1}{2} u^-_{i+\frac{1}{2}} h_x \left(1 - \frac{\phi(r^-_{i+\frac{1}{2}})}{r^-_{i+\frac{1}{2}}} \right), \tag{3.12}$$

where $\phi(r)$ is defined by (2.6c) and $u^+_{i+\frac{1}{2}}, u^-_{i+\frac{1}{2}}, r^+_{i+\frac{1}{2}}$ and $r^-_{i+\frac{1}{2}}$ are defined in the appendix. Both the explicit SGS diffusion term, and the implicit diffusion term are depicted in figure 5. Although the two terms are not identical (the implicit diffusion term appears to act on smaller scales), there is a close correspondence. These results confirm the findings of Boris *et al.* (1992) that a SGS model is not essential for monotone schemes. Here we will give a short explanation of the behaviour of the limited $\kappa = -1$ scheme. For small t, the scalar field is still smooth. As a consequence in most regions the upwind ratio of consecutive scalar gradients r, and the limiter function $\phi(r)$ are approximately equal to one, which according to (3.12) implies $D^{art} \approx 0$. Hence there is initially almost no dissipation of scalar variance. However, for increasing t smaller scales appear, and r deviates strongly from one in more and more grid points. According to (2.6c), D^{art} becomes positive for most (but not all) of these grid points. The positive D^{art} dissipates small-scale variance, thus bringing r and $\phi(r)$ again closer to one. So the limited $\kappa = -1$ scheme tries to balance the production of small-scale variance (which is determined mainly by the resolved large-scale field) with a dissipation term which is similar to the explicit SGS diffusion term that we derived in section 1.1.

The volume-integrated variance should decrease in time because we use periodic boundary conditions (3.1), for which there is no contribution of the boundary of the domain in (1.24). Since it can be shown that the second-order central scheme conserves resolved variance, and the added SGS diffusion term only dissipates resolved variance, we expect that the TVD property is not violated if the second-order central scheme is used. This is confirmed by figure 6, which shows the volume-integrated variance as a function of time for the second-order central scheme with SGS model. Notice how for increasing resolution more and more of the variance is resolved. Although with the finest resolution it is still not possible to resolve all scales (the turbulent diffusivity D_t is 2.5 times larger than D for this resolution), most of the scales are resolved. In figures 8 through 13 we will use this fine resolution result as a reference. The second-order central scheme is not monotone, and as a consequence positivity is not guaranteed. In fact negative values were found for the runs with a resolution of $64 \times 65 \times 65$ and $128 \times 129 \times 129$ cells. Figure 7 shows the global minimum of c as a function of time for the run with a resolution of $128 \times 129 \times 129$ cells. Notice that (significant) negative values do not appear immediately, since for small t the scalar field is smooth, and hence numerical errors are small.

The effect of the constant C_2, which appears in the expression for the SGS eddy diffusivity D_t, is shown in figure 8 for a resolution of $32 \times 33 \times 33$ cells and the second-order central scheme. If no SGS model is used, i.e. $C_2 = 0$, the resolved variance is much too large. This demonstrates the need for a

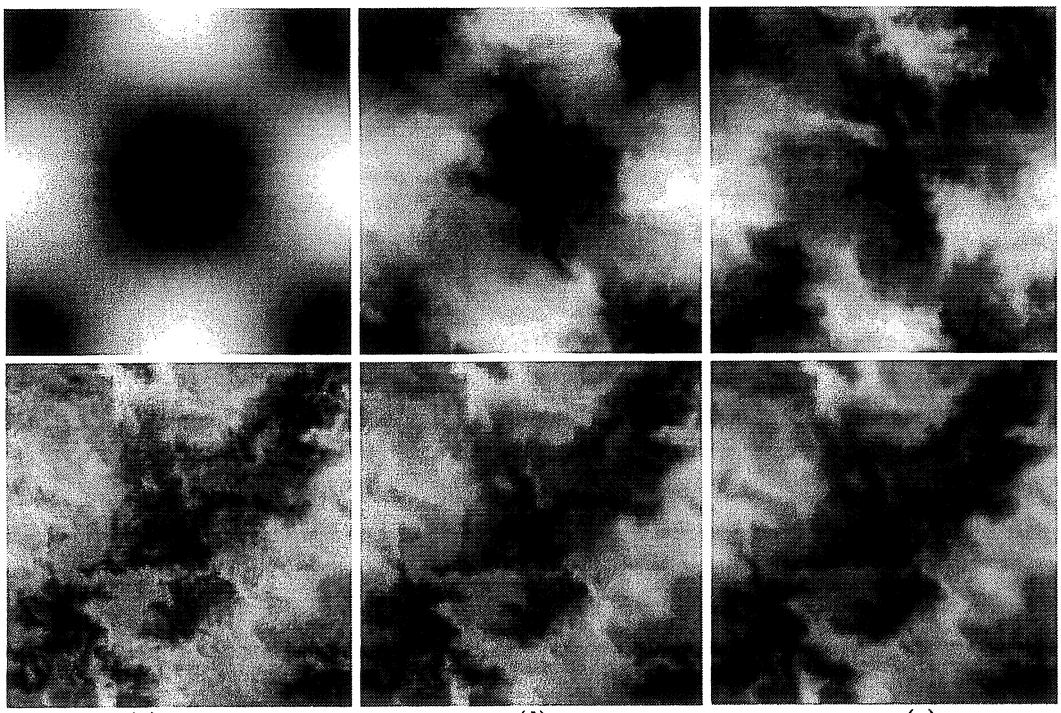

Figure 4: The scalar field at $x = 0.5$ for a resolution of $128 \times 129 \times 129$ cells. **Top panel:** (a) At $t = 0$, (b) $t = 0.18$ and (c) $t = 0.36$ for the 2nd-order central scheme with subgrid-scale model ($C_2 = 2$). **Lower panel:** The 2nd-order central scheme (a) without subgrid-scale model, (b) with subgrid-scale model ($C_2 = 2$) and (c) the limited $\kappa = -1$ scheme without subgrid-scale model at $t = 0.86$.

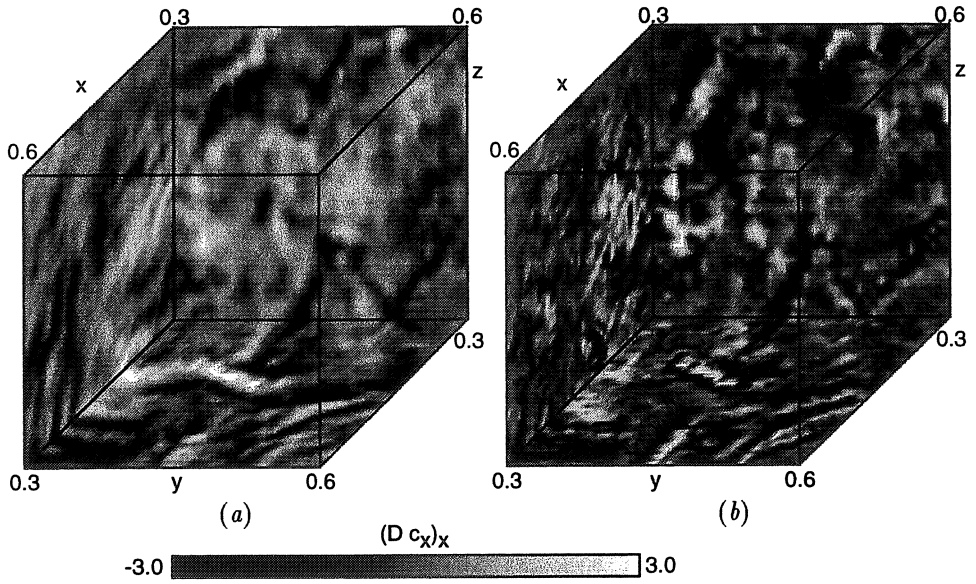

Figure 5: (a) Explicit (2nd-order central with subgrid-scale model / $C_2 = 2$) and (b) implicit (limited $\kappa = -1$ scheme without subgrid-scale model) diffusion term. Both for a resolution of $128 \times 129 \times 129$ cells and at $t = 0.86$. Note that this plot shows only part of the domain.

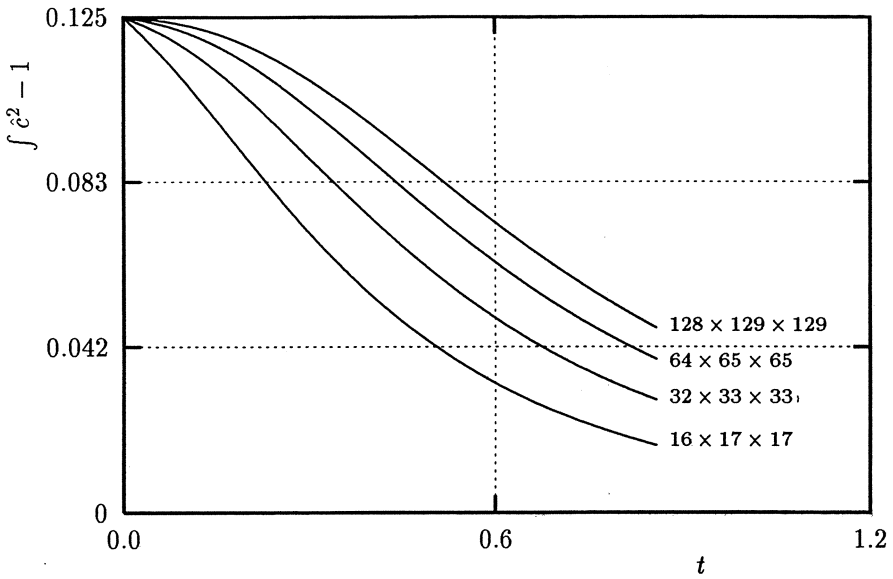

Figure 6: Volume-integrated resolved variance as a function of time for the second-order central scheme (2.3) with subgrid-scale model (using the typical value $C_2 = 2$). Results are shown for four different resolutions.

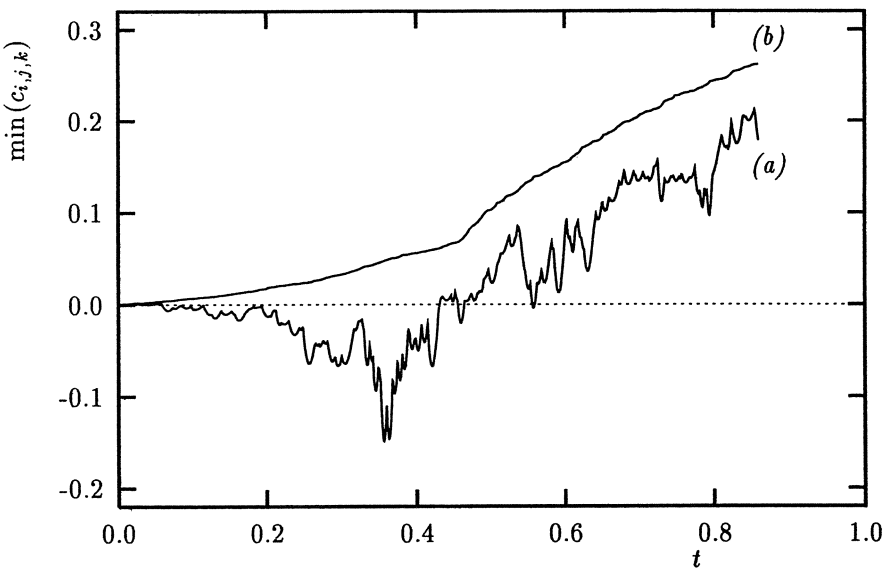

Figure 7: Minimum of c as a function of time for *(a)* the second-order central scheme (2.3) with subgrid-scale model ($C_2 = 2$) and *(b)* the limited $\kappa = -1$ scheme (2.6) without subgrid-scale model ($C_2 = 0$) (resolution: 128 x 129 x 129 cells).

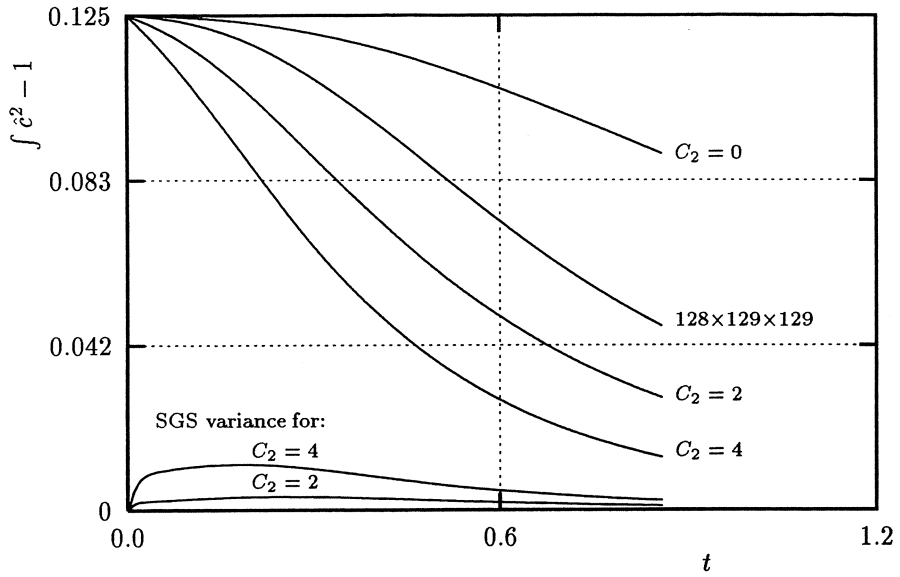

Figure 8: Volume-integrated resolved variance, and SGS variance, as a function of time for the second-order central scheme (2.3) and a resolution of $32 \times 33 \times 33$ cells. Results are shown for different C_2. For $C_2 = 2$ the fine resolution result ($128 \times 129 \times 129$) is also shown.

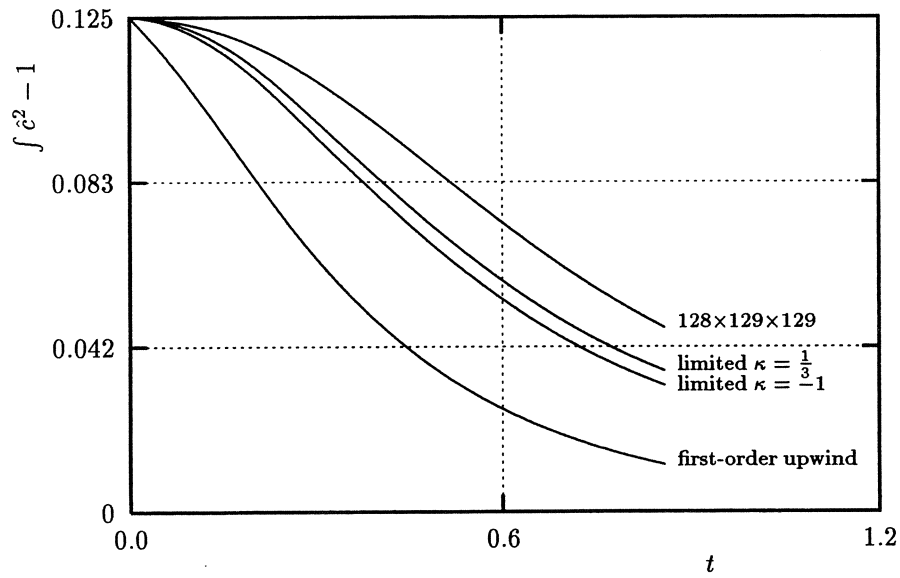

Figure 9: Volume-integrated resolved variance as a function of time and a resolution of $32 \times 33 \times 33$ cells. Results are shown for the first-order upwind scheme (2.4), the limited $\kappa = \frac{1}{3}$ scheme (2.5) and the limited $\kappa = -1$ scheme (2.6), all without subgrid-scale model ($C_2 = 0$). Again the fine resolution result, shown in the previous figures, is included.

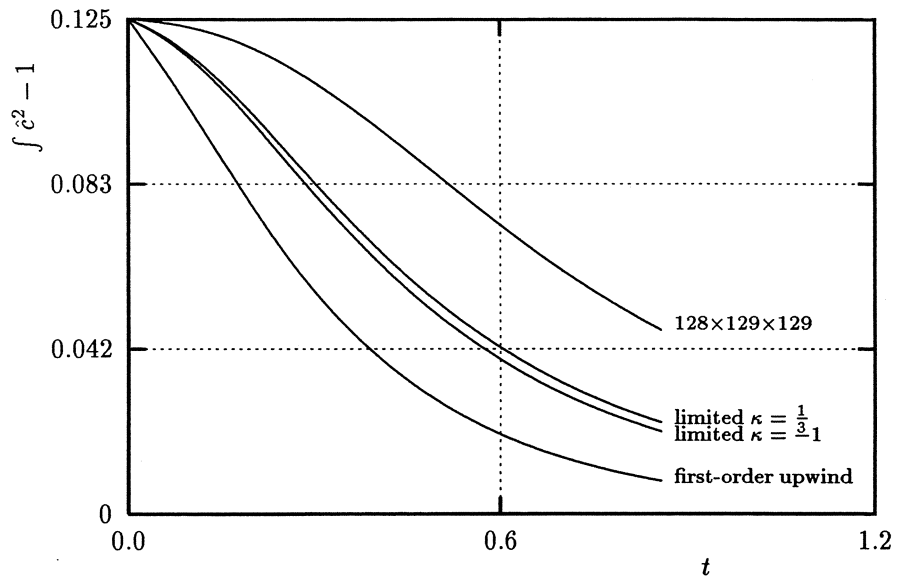

Figure 10: As in figure 9, but now with subgrid-scale model ($C_2 = 2$).

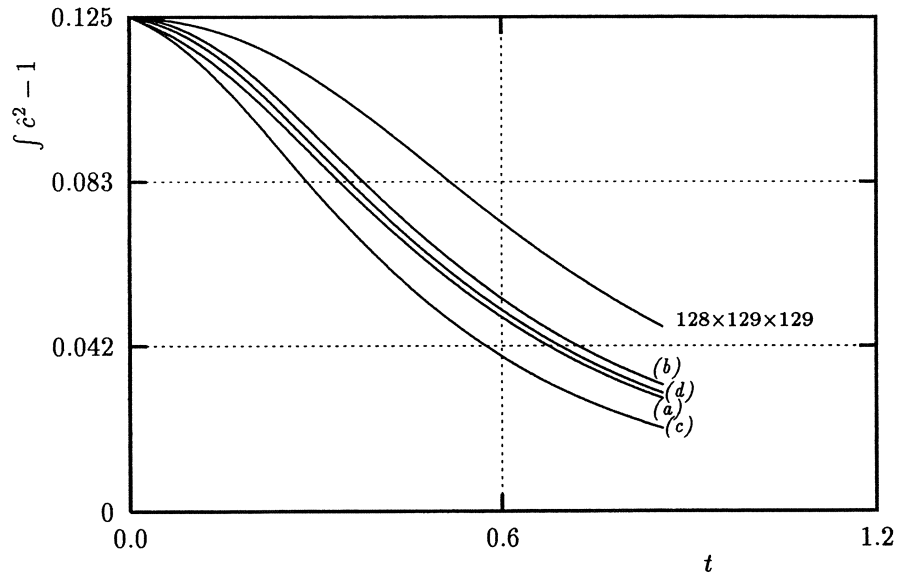

Figure 11: Volume-integrated resolved variance as a function of time for a resolution of $32 \times 33 \times 33$ cells. Results are shown for *(a)* the 2nd-order central scheme (2.3) with subgrid-scale model, *(b)* the limited $\kappa = -1$ scheme (2.6c) without and *(c)* with subgrid-scale model and *(d)* the new MILES scheme (2.10) with limiter (2.24). Again the fine resolution result, shown in the previous figures, is included.

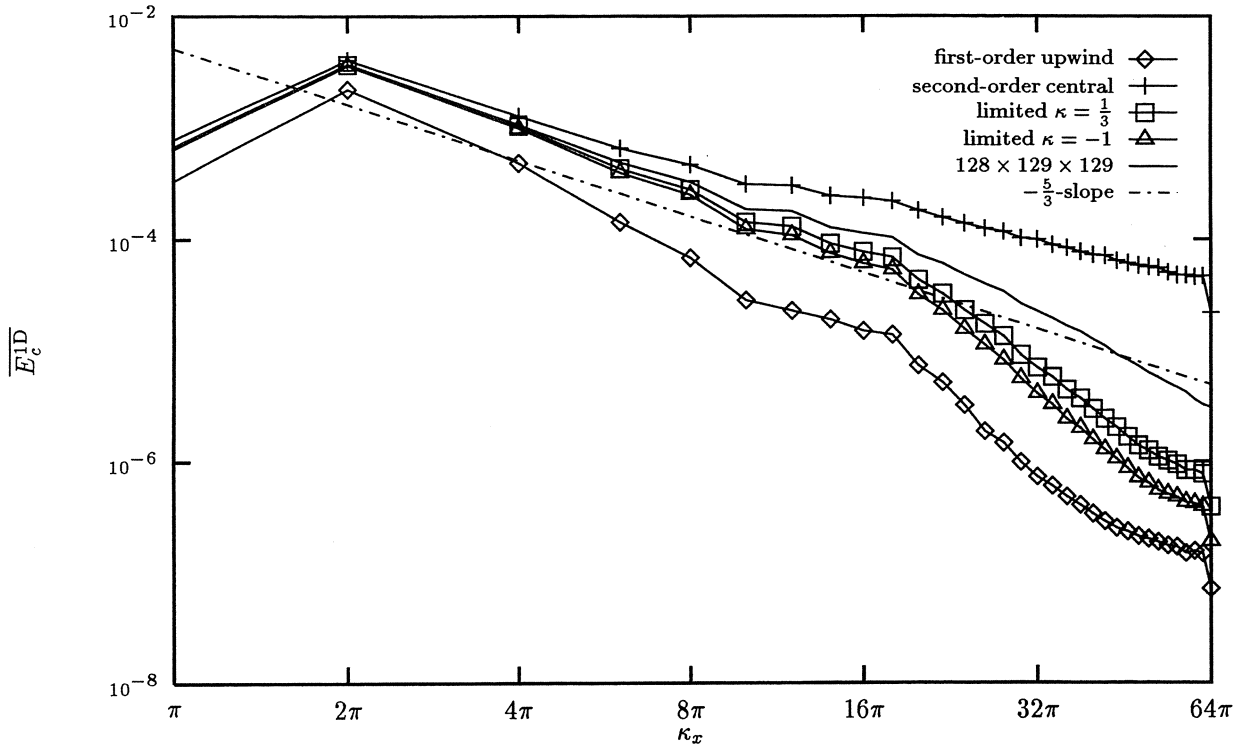

Figure 12: Averaged (in y, z-direction at $t = 0.86$) 1-D spectra of scalar variance for $C_2 = 0$ (no subgrid-scale model) and a resolution of $64 \times 65 \times 65$ cells.

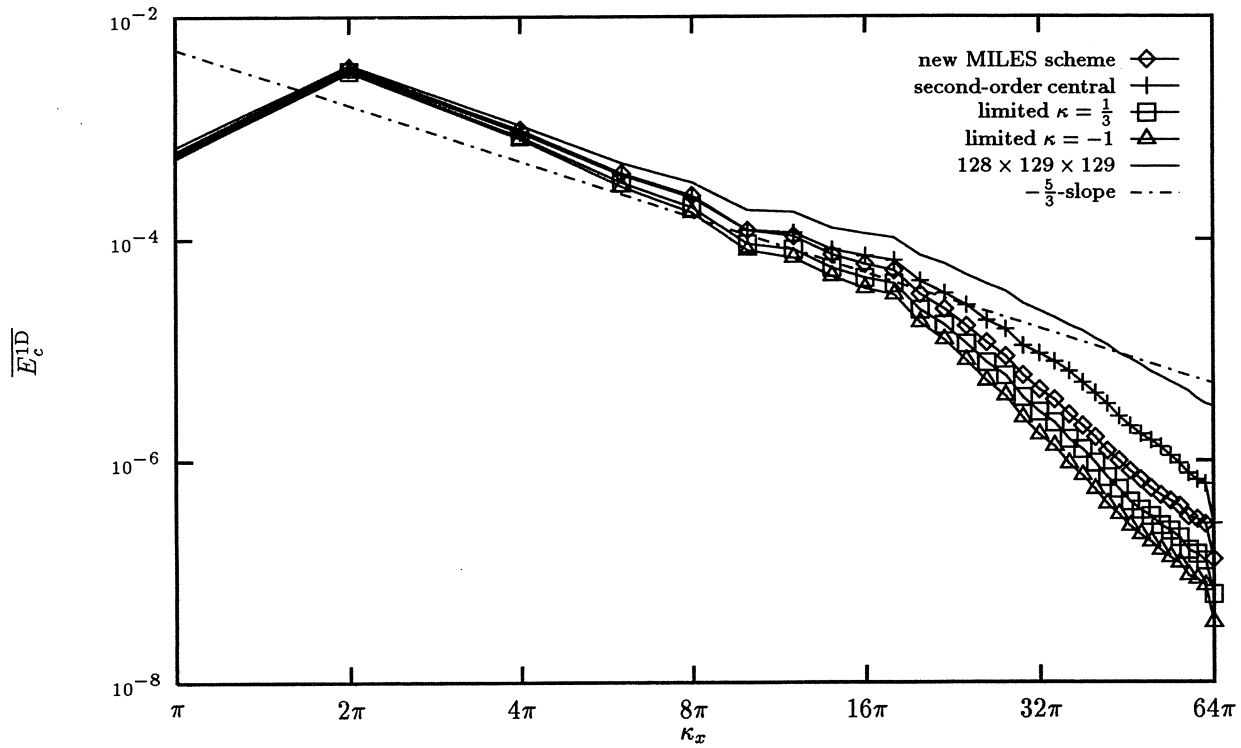

Figure 13: Averaged (in y, z-direction at $t = 0.86$) 1-D spectra of scalar variance for $C_2 = 2$ and a resolution of $64 \times 65 \times 65$ cells.

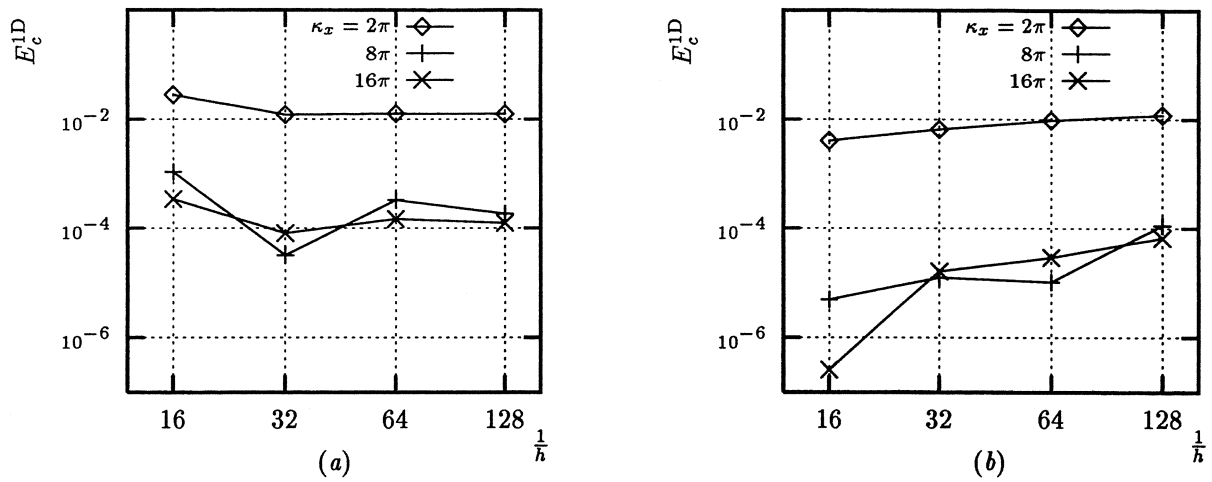

Figure 14: Convergence of E_c^{1D} (at $y, z = 0.5$, $t = 0.86$) with increasing resolution for three different wave numbers. For the second-order central scheme (2.3) without (a) and with (b) subgrid-scale model ($C_2 = 2$).

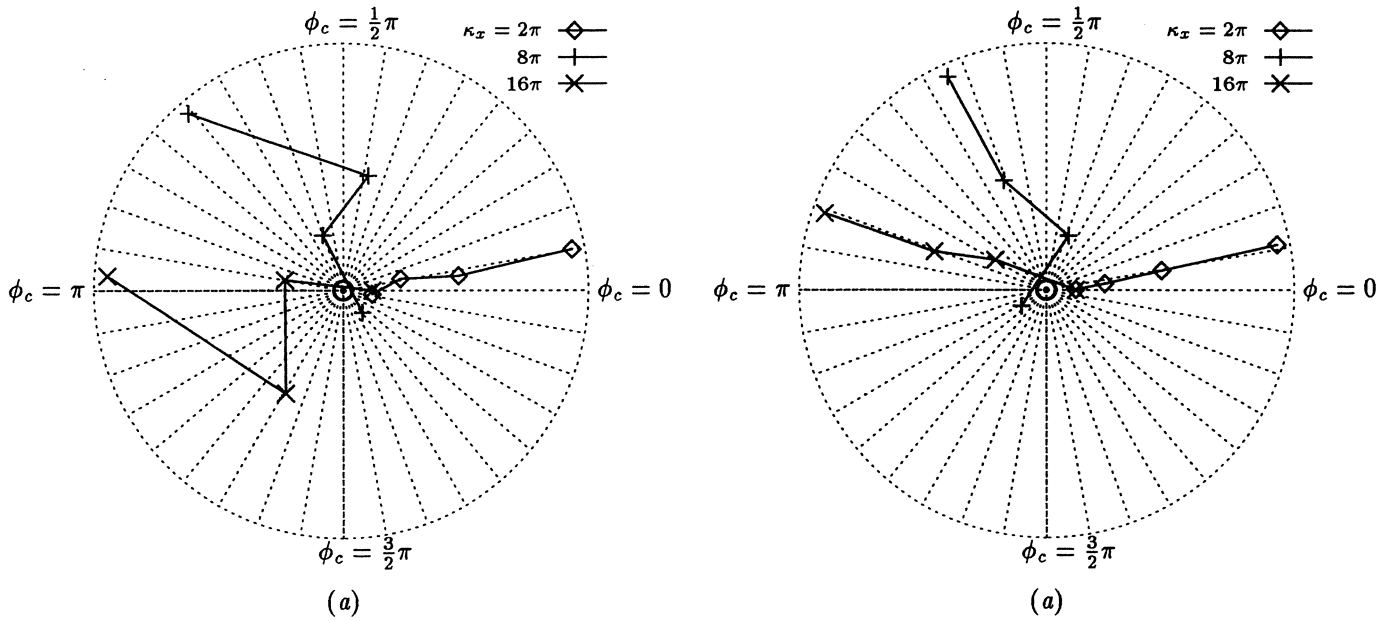

Figure 15: Polar plot of the convergence of phase ϕ_c (at $y, z = 0.5$, $t = 0.86$) with increasing resolution for three different wave numbers. The coordinate in radial direction is used for $\frac{1}{h}$. For the second-order central scheme (2.3) without (a) and with (b) subgrid-scale model ($C_2 = 2$).

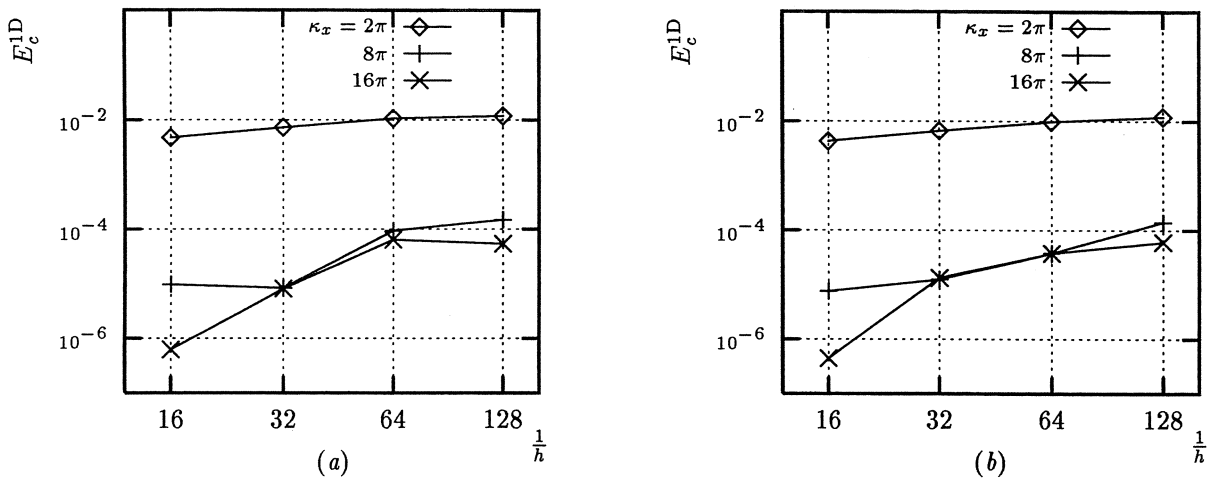

Figure 16: Convergence of E_c^{1D} (at $y, z = 0.5$, $t = 0.86$) with increasing resolution for three different wave numbers. (a) For the limited $\kappa = -1$-scheme (2.6) without subgrid-scale model and (b) for the new MILES scheme (2.10) with limiter (2.24).

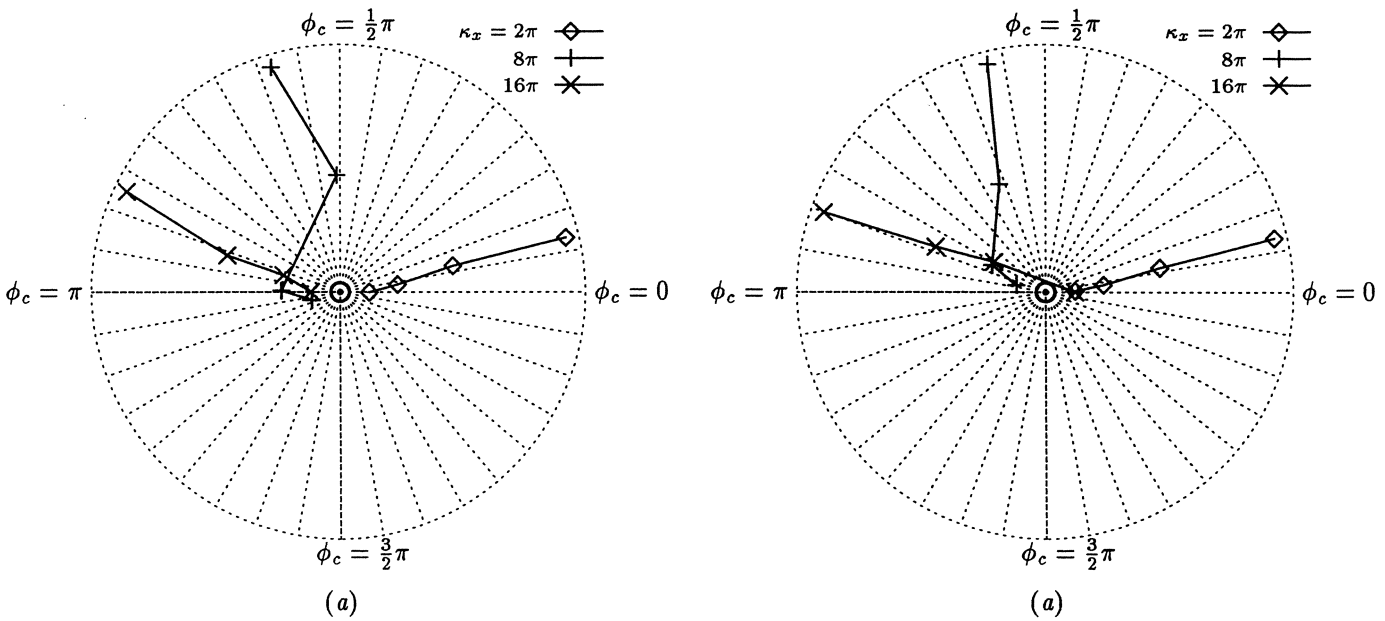

Figure 17: Polar plot of the convergence of phase ϕ_c (at $y, z = 0.5$, $t = 0.86$) with increasing resolution for three different wave numbers. The coordinate in radial direction is used for $\frac{1}{h}$. (a) For the limited $\kappa = -1$-scheme (2.6) without subgrid-scale model and (b) for the new MILES scheme (2.10) with limiter (2.24).

SGS model if the standard second-order central scheme is used. The runs with a SGS model ($C_2 = 2$ and $C_2 = 4$) both yield smaller resolved variances than the fine resolution result, indicating that, especially for $C_2 = 4$, a substantial part of the variance is SGS variance. Although the SGS model improves the large-scale solution, the estimate of the SGS variance (1.21) is not very accurate (see figure 8). Relation (1.21) gives too little variance for large t. As we will discuss later, this deficiency is mainly because the spatial filter introduced in section 1.1 is not a Fourier cut-off filter (which is assumed in (1.21)).

Figure 9 again shows the volume-integrated variance as a function of time, but now for three different monotone schemes, and no SGS model. Unlike the second-order central scheme, none of the monotone schemes yields too much variance. As mentioned before, this is due to the fact that the monotone schemes add an implicit diffusion term. The results obtained with the first-order upwind scheme (2.4) are extremely diffusive. This behaviour can be explained from (3.11) and (3.12), which yield $D^{art} = \frac{1}{2}|u|h$ for the first-order upwind scheme. So the first-order upwind scheme *always* adds an $O(h)$ artificial diffusivity compared to the second-order central scheme. Thus an important advantage of the limited κ-schemes (2.5) and (2.6), compared to the first-order upwind scheme, is that these schemes only add an implicit diffusion term when necessary. This is especially evident for small t, where the limited κ-schemes detect that the scalar field is smooth and introduce no artificial diffusivity. The performance of the limited κ-schemes is comparable with that of the second-order central scheme with SGS model. The former are even slightly less dissipative. However, a more important advantage of the limited κ-schemes is there monotone behaviour, which ensures positivity (see figure 7).

A disadvantage of the limited κ-schemes without SGS model is the inability to obtain an estimate of SGS quantities. Therefore, we will now consider the limited κ-schemes *with* SGS model. The results, depicted in figure 10, are much more dissipative. This indicates that, although the explicit SGS diffusion term removes the smallest scales, the limited κ-schemes still add a substantial implicit diffusion term to satisfy the monotonicity requirement. As a remedy we have developed in section 2.2 advection schemes which directly combine the monotonicity device and the physical SGS term. Figure (11) shows results obtained with the new MILES scheme (2.10) with limiter (2.24), and some of the aforementioned schemes. The new MILES scheme performs reasonably well; unlike the limited κ-schemes with SGS model, it is not much more dissipative than the second-order central scheme. This suggests that almost all the dissipation of variance can be attributed to the physical $O(h^{\frac{4}{3}})$ diffusion.

To obtain information on the different scales of the scalar field, we have plotted in figures 12 and 13 averaged one-dimensional power spectra for respectively $C_2 = 0$ and $C_2 = 2$. The $-\frac{5}{3}$-slope in these figures is the theoretical slope in the inertial-convective subrange, given by (1.8b). The dissipation rate of variance that appears in this equation has been estimated from the decrease in volume-integrated variance found for the fine $128 \times 129 \times 129$ resolution runs. Since the Reynolds number of the flow field is rather low, it is questionable whether the $-\frac{5}{3}$-slope can be expected to extend over a large range of wave numbers. Nevertheless most of the results are reasonably close to the $-\frac{5}{3}$-slope for $2\pi \leq \kappa_x \leq 16\pi$. Figure 12 shows that the first-order upwind scheme without SGS model is too dissipative for all wave numbers. The second-order central scheme without SGS model is not dissipative enough for all wave numbers, especially at the smaller scales where there is a build-up of variance. The limited κ-schemes give much better results, in agreement with previous results. Notice that these schemes especially damp wave numbers larger than 16π, which is a wanted property because these wave numbers cannot be solved accurately. From figure 13 it is clear that also the second-order central scheme with SGS model damps variance at large wave numbers. Comparing the $64 \times 65 \times 65$-grid results with the fine resolution result, reveals that not only the smallest scales are filtered. A substantial part of the SGS variance is located at large scales. This explains why (1.21), which integrates the variance spectrum between κ_c and κ_u, underestimates the SGS variance. The limited κ-schemes with SGS model, show a larger dissipation at all wave numbers than the limited κ-schemes without SGS model. Only for $\kappa_x = 2\pi$, the variance is more or less the same as for the second-order central scheme with, and the limited κ-schemes without SGS model. The new MILES scheme performs much better, showing a good correspondence with these results for $\kappa_x \leq 12\pi$.

A more detailed comparison between the standard second-order central scheme (with and without SGS model), the limited $\kappa = -1$ scheme without SGS model and the new MILES scheme is presented in figures 14 through 17. These figures show the convergence, for increasing resolution, of the one-dimensional variance, and phase spectrum, at $y, z = 0.5$ and $t = 0.86$ for three different wave numbers

scheme	CPU time (s)	Mflops
second-order central	0.25	416
first-order upwind	0.34	412
limited $\kappa = \frac{1}{3}$	1.25	407
limited $\kappa = -1$	1.02	401
new MILES scheme	1.16	409

Table 1: Required CPU time per time step on a Cray C90 for the different spatial discretizations (resolution: $128 \times 129 \times 129$ cells).

($2\pi, 8\pi$ and 16π). The second-order central scheme without SGS model has a poor performance. E.g. for a resolution of $64 \times 65 \times 65$ cells, the phase for $\kappa_x = 8\pi$ is still very inaccurate, despite the fact that the resolution should be sufficient to resolve this wave number. Furthermore the energy at this wave number is too large. The other three schemes give better results, although they are quite dissipative. E.g. for $\kappa_x = 2\pi$ there is still an increase in energy at the finest resolution, despite the fact that this resolution should be more than sufficient (which is confirmed by the close correspondence of the phase for the three different schemes). The second-order central scheme with SGS model and the new MILES scheme have a somewhat better convergence behaviour for the phase ϕ_c.

Table 1 shows the required CPU time (per time step) on a Cray C98 for the different spatial discretizations and a resolution of 128×129×129 cells. The numerical schemes which guarantee monotonicity are approximately four to five times as expensive as the standard second-order central scheme (except for the extremely diffusive first-order upwind scheme). This factor will be somewhat smaller on scalar machines (≈ 3). Notice that the new MILES scheme does not require significantly more CPU time than the existing limited κ-schemes. More than 50% of the CPU time (4.83 CPU seconds per time step at 684 Million FLoating-point OPerations per Second) was required for the kinematic simulation.

4 Conclusions

The standard large-eddy simulation (LES) approach, in which the continuous equations are first filtered, and then solved using straightforward discretizations, does not guarantee that certain physical properties of the exact solution are satisfied. Monotone spatial discretizations were used in this paper to guarantee the (physical) monotonicity property (in the sense of Spekreijse, 1987) for the conservation equation of a passive scalar. In accordance with the findings of Boris *et al.* (1992), we found that the (monotone) limited κ-schemes already give good results without a subgrid-scale (SGS) term (which enters the conservation equation of the scalar after filtering). The monotone schemes add an implicit diffusion term, which filters scales for which the resolution is too low. For the second-order central scheme, which does not add an implicit diffusion term, an explicit SGS diffusion term is necessary to obtain an accurately resolved scalar field.

Although the limited κ−schemes give good results without a SGS model, it is still necessary to introduce a SGS model if an accurate LES is wished for; only if a SGS model is used, an estimate of SGS quantities can be obtained. We found that simply combining the limited κ-schemes and the explicit SGS diffusion term gives results which are more dissipative than those obtained with the second-order central scheme with SGS diffusion term. This indicates that, although the explicit SGS diffusion term filters the smallest scales, the monotone schemes still add an implicit diffusion term to guarantee monotonicity. An alternative monotone scheme, which introduces the SGS model in the discrete equations, gives a better performance. This new MILES scheme, which is monotone and uses an implicit SGS diffusion term, is almost as dissipative as the standard second-order central scheme with explicit SGS diffusion term.

A further step would be to analyze in more detail the ratio of the (explicit or implicit) SGS term and the term which is added to guarantee monotonicity. In an ideal situation, the former would be much larger than the latter, since the subgrid-scale model should effectively filter in such a way that numerical errors are small. Situations in which this condition is violated are interesting, because they suggest that either the SGS model fails, or the monotone scheme imposes monotonicity conditions which

are too strict.

Acknowledgments

The investigations were in part supported by the Netherlands Geoscience Foundation (GOA) with financial aid from the Netherlands Organization for Scientific Research (NWO). The use of supercomputing facilities was sponsored by the National Computing Facilities Foundation (NCF).

Appendix

Spekreijse (1987) derived a class of spatial discretizations which guarantee monotonicity for the following nonlinear scalar conservation law

$$\frac{\partial c}{\partial t} + \frac{\partial f(c)}{\partial x} + \frac{\partial g(c)}{\partial y} + \frac{\partial h(c)}{\partial z} = 0. \tag{4.1}$$

In here he splitted the flux function $f(c)$ (and similarly $g(c)$, $h(c)$) such that

$$f(c) = f^+(c) + f^-(c), \tag{4.2a}$$

$$\frac{\mathrm{d}f^+(c)}{\mathrm{d}c} \geq 0\,, \quad \frac{\mathrm{d}f^-(c)}{\mathrm{d}c} \leq 0. \tag{4.2b}$$

The semi-discrete conservation equation for c can then be written as (using the finite-volume technique)

$$\begin{aligned}\frac{\mathrm{d}c_{i,j,k}}{\mathrm{d}t} = \quad & \frac{f^-_{i-\frac{1}{2},j} - f^-_{i+\frac{1}{2},j}}{c^-_{i-\frac{1}{2},j} - c^-_{i+\frac{1}{2},j}} \frac{c^-_{i-\frac{1}{2},j} - c^-_{i+\frac{1}{2},j}}{\delta c^-_i} \delta c^-_i + \frac{f^+_{i-\frac{1}{2},j} - f^+_{i+\frac{1}{2},j}}{c^+_{i-\frac{1}{2},j} - c^+_{i+\frac{1}{2},j}} \frac{c^+_{i-\frac{1}{2},j} - c^+_{i+\frac{1}{2},j}}{\delta c^+_i} \delta c^+_i + \\ & \frac{g^-_{i,j-\frac{1}{2}} - g^-_{i,j+\frac{1}{2}}}{c^-_{i,j-\frac{1}{2}} - c^-_{i,j+\frac{1}{2}}} \frac{c^-_{i,j-\frac{1}{2}} - c^-_{i,j+\frac{1}{2}}}{\delta c^-_j} \delta c^-_j + \frac{g^+_{i,j-\frac{1}{2}} - g^+_{i,j+\frac{1}{2}}}{c^+_{i,j-\frac{1}{2}} - c^+_{i,j+\frac{1}{2}}} \frac{c^+_{i,j-\frac{1}{2}} - c^+_{i,j+\frac{1}{2}}}{\delta c^+_j} \delta c^+_j,\end{aligned} \tag{4.3}$$

where δc^-_i, δc^+_i, δc^-_j and δc^+_j are

$$\delta c^-_i \equiv c_{i+1,j} - c_{i,j} \tag{4.4a}$$

$$\delta c^+_i \equiv c_{i-1,j} - c_{i,j} \tag{4.4b}$$

$$\delta c^-_j \equiv c_{i,j+1} - c_{i,j} \tag{4.4c}$$

$$\delta c^+_j \equiv c_{i,j-1} - c_{i,j}, \tag{4.4d}$$

(For reasons of clarity we consider the two-dimensional case and use $h_x = h_y = 1$, with h_x and h_y the grid distances in x- and y-direction respectively.) Following (1.25) and (1.26), monotonicity is guaranteed if

$$\begin{aligned}0 \leq \frac{c^-_{i+\frac{1}{2},j} - c^-_{i-\frac{1}{2},j}}{c_{i+1,j} - c_{i,j}} \leq M \quad \wedge \quad 0 \leq \frac{c^+_{i+\frac{1}{2},j} - c^+_{i-\frac{1}{2},j}}{c_{i,j} - c_{i-1,j}} \leq M \quad \wedge \\ 0 \leq \frac{c^-_{i,j+\frac{1}{2}} - c^-_{i,j-\frac{1}{2}}}{c_{i,j+1} - c_{i,j}} \leq M \quad \wedge \quad 0 \leq \frac{c^+_{i,j+\frac{1}{2}} - c^+_{i,j-\frac{1}{2}}}{c_{i,j} - c_{i,j-1}} \leq M \quad \text{where } M \in (0,\infty),\end{aligned} \tag{4.5}$$

since (4.2) implies

$$\begin{aligned}\frac{f^-_{i-\frac{1}{2},j} - f^-_{i+\frac{1}{2},j}}{c^-_{i-\frac{1}{2},j} - c^-_{i+\frac{1}{2},j}} \leq 0 \quad \wedge \quad \frac{f^+_{i-\frac{1}{2},j} - f^+_{i+\frac{1}{2},j}}{c^+_{i-\frac{1}{2},j} - c^+_{i+\frac{1}{2},j}} \geq 0 \quad \wedge \\ \frac{g^-_{i,j-\frac{1}{2}} - g^-_{i,j+\frac{1}{2}}}{c^-_{i,j-\frac{1}{2}} - c^-_{i,j+\frac{1}{2}}} \leq 0 \quad \wedge \quad \frac{g^+_{i,j-\frac{1}{2}} - g^+_{i,j+\frac{1}{2}}}{c^+_{i,j-\frac{1}{2}} - c^+_{i,j+\frac{1}{2}}} \geq 0.\end{aligned} \tag{4.6}$$

Here, as well as in Spekreijse (1987), the following class of cell-face interpolations is considered for $c^-_{i+\frac{1}{2},j}$ and $c^+_{i+\frac{1}{2},j}$ (and similarly for $c^-_{i-\frac{1}{2},j}, c^+_{i-\frac{1}{2},j}, c^-_{i,j+\frac{1}{2}}, c^+_{i,j+\frac{1}{2}}, c^-_{i,j-\frac{1}{2}}, c^+_{i,j-\frac{1}{2}}$)

$$c^-_{i+\frac{1}{2},j} = c_{i+1,j} + \frac{1}{2}\phi\left(r^-_{i+\frac{1}{2}}\right)(c_{i+1,j} - c_{i+2,j}) \tag{4.7a}$$

$$c^+_{i+\frac{1}{2},j} = c_{i,j} + \frac{1}{2}\phi\left(r^+_{i+\frac{1}{2}}\right)(c_{i,j} - c_{i-1,j}), \tag{4.7b}$$

where ϕ is the so-called limiter function and $r^-_{i+\frac{1}{2}}$ and $r^+_{i+\frac{1}{2}}$ are upwind ratios of consecutive solution gradients:

$$r^-_{i+\frac{1}{2}} = \frac{c_{i,j} - c_{i+1,j}}{c_{i+1,j} - c_{i+2,j}} \tag{4.8a}$$

$$r^+_{i+\frac{1}{2}} = \frac{c_{i+1,j} - c_{i,j}}{c_{i,j} - c_{i-1,j}}. \tag{4.8b}$$

Substituting the cell-face interpolations (4.7) into (4.5) yields the following monotonicity requirements for the limiter function:

$$\alpha \le \phi(r) \le M \quad \wedge \quad -M \le \frac{\phi(r)}{r} \le 2 + \alpha \quad \text{where } M \in (0,\infty) \ \wedge \ \alpha \in [-2,0]. \tag{4.9}$$

For the conservation equation (1.1) the flux functions in (4.1) are *also* a function of the velocity field:

$$f(u,c) = uc \tag{4.10a}$$

$$g(v,c) = vc. \tag{4.10b}$$

We take the following decomposition for $f(u,c)$ (and similarly for $g(v,c)$) at the cell-face $i+\frac{1}{2}$,

$$f_{i+\frac{1}{2},j} = u^-_{i+\frac{1}{2}} c^-_{i+\frac{1}{2}} + u^+_{i+\frac{1}{2}} c^+_{i+\frac{1}{2}}, \quad \text{where } u^-_{i+\frac{1}{2}} \equiv \min(0, u_{i+\frac{1}{2}}),\ u^+_{i+\frac{1}{2}} \equiv \max(0, u_{i+\frac{1}{2}}), \tag{4.11}$$

which is consistent with (4.2). We continue by substituting the cell-face interpolations (4.7) and the flux function decomposition (4.11) into the semi-discrete equation for c (4.3), and assume a solenoidal velocity field, to obtain

$$\begin{aligned}\frac{\mathrm{d}c_{i,j,k}}{\mathrm{d}t} = \; & -u^-_{i+\frac{1}{2},j}\left(1 + \frac{1}{2}L_{i,j} - \frac{\phi\left(r^-_{i+\frac{1}{2}}\right)}{2r^-_{i+\frac{1}{2}}}\right)\delta c^-_i + u^+_{i-\frac{1}{2},j}\left(1 + \frac{1}{2}L_{i,j} - \frac{\phi\left(r^+_{i-\frac{1}{2}}\right)}{2r^+_{i-\frac{1}{2}}}\right)\delta c^+_i \\ & -v^-_{i,j+\frac{1}{2}}\left(1 + \frac{1}{2}L_{i,j} - \frac{\phi\left(r^-_{j+\frac{1}{2}}\right)}{2r^-_{j+\frac{1}{2}}}\right)\delta c^-_j + v^+_{i,j-\frac{1}{2}}\left(1 + \frac{1}{2}L_{i,j} - \frac{\phi\left(r^+_{j-\frac{1}{2}}\right)}{2r^+_{j-\frac{1}{2}}}\right)\delta c^+_j. \end{aligned} \tag{4.12}$$

In here $L_{i,j}$ is given by

$$L_{i,j} = \frac{u^+_{i+\frac{1}{2},j}\delta c^+_i \phi\left(r^+_{i+\frac{1}{2}}\right) - u^-_{i-\frac{1}{2},j}\delta c^-_i \phi\left(r^-_{i-\frac{1}{2}}\right) + v^+_{i,j+\frac{1}{2}}\delta c^+_j \phi\left(r^+_{j+\frac{1}{2}}\right) - v^-_{i,j-\frac{1}{2}}\delta c^-_j \phi\left(r^-_{j-\frac{1}{2}}\right)}{u^+_{i-\frac{1}{2},j}\delta c^+_i - u^-_{i+\frac{1}{2},j}\delta c^-_i + v^+_{i,j-\frac{1}{2}}\delta c^+_j - v^-_{i,j+\frac{1}{2}}\delta c^-_j}. \tag{4.13}$$

Now monotonicity requires that

$$0 \le 1 + \frac{1}{2}L_{i,j} - \frac{\phi(r)}{2r} \le M \quad \text{where } M \in (0,\infty). \tag{4.14}$$

If $\phi(r)$ can be negative, then (4.13) shows that $L_{i,j} \in (-\infty, +\infty)$, in which case (4.14) cannot be satisfied. However, if $\forall r\ \phi(r) \ge 0$, then $L_{i,j} \ge 0$ at local minima and maxima. A sufficient condition for monotonicity is therefore

$$0 \le \phi(r) \le M \quad \wedge \quad -M \le \frac{\phi(r)}{r} \le 2 \quad \text{where } M \in (0,\infty). \tag{4.15}$$

Hence, our monotonicity condition is the Spekreijse condition (4.9) with $\alpha = 0$.

References

[1] ANDREAS, E.L. 1987 Spectral measurements in a disturbed boundary layer over snow. *J. Atmos. Sci.* **44**, 1912-1939.

[2] BORIS, J.P., GRINSTEIN, F.F., ORAN, E.S. & KOLBE, R.L. 1992 New insights into large eddy simulation. *Fluid Dynamics Research* **10**, 199-228.

[3] CHASE, D.M. 1970 Space-time correlations of velocity and pressure and the role of convective homogeneous turbulence in the universal range. *Acustica* **22**, 303-320.

[4] CIOFALO, M. 1993 Large-eddy simulation of turbulent flow and heat transfer: a state of the art review. Department of Nuclear Engineering, University of Palermo, Italy.

[5] DEARDORFF, J.W. 1970 A numerical study of three-dimensional turbulent channel flow at large Reynolds numbers. *J. Fluid Mech.* **41**, 453-480.

[6] EGGELS, J.G.M. 1994 Direct and large eddy simulation of turbulent flow in a cylindrical pipe geometry. Delft University.

[7] FUNG, J.C.H., HUNT, J.C.R., MALIK, N.A. & PERKINS, R.J. 1992 Kinematic simulation of homogeneous turbulence by unsteady random Fourier modes. *J. Fluid Mech.* **236**, 281-318.

[8] HINZE, J.O. 1975 *Turbulence.* McGraw-Hill.

[9] KOREN, B. 1993 A robust upwind discretization method for advection, diffusion and source terms. In *Notes on Numerical Fluid Mechanics* **45** (eds. C.B. Vreugdenhil & B. Koren), pp. 117-138. Vieweg.

[10] LEER, B. VAN 1985 Upwind-difference methods for aerodynamic problems governed by the Euler equations. In *Lectures in Applied Mathematics* **22 – Part 2** (eds. B.E. Engquist, S. Osher & R.C.J. Somerville), pp. 327-336. American Mathematical Society.

[11] MASON, P. J. 1994 Large-eddy simulation: a critical review of the technique, *Q. J. R. Meteorol. Soc.* **120**, 1-26.

[12] SPEKREIJSE, S.P. 1987 Multigrid solution of monotone second-order discretizations of hyperbolic conservation laws. *Math. Comput.* **49**, 135-155.

[13] SWEBY, P.K. 1984 High resolution schemes using flux limiters for hyperbolic conservation laws. *SIAM J. Numer. Anal.* **21**, 995-1011.

[14] TENNEKES, H. & LUMLEY, J.L. 1980 *A First Course in Turbulence.* The MIT Press.

Contents